Environmental controls on silica sinter formation revealed by radiocarbon dating

Silvina Slagter, Martin Reich, Carolina Munoz-Saez, John Southon, Diego Morata, Fernando Barra, Jian Gong, John Roma Skok.

Figure DR1. Paleosinter textures. A and B correspond to mound 502. A. Contact between geyserite in the lower part and palisade in the upper part. B. Increased magnification photo of the rectangle in A. See hammer for scale. C and D correspond to mound 404. C. Contact between laminated and palisade texture. D. Porous palisade texture. Magnification of the rectangle in C. See coin for scale.E and F are hand specimens of textures in mounds 404 and 502. E. Palisade texture in sample 404f. F. Geyserite texture corresponding to sample 502m.

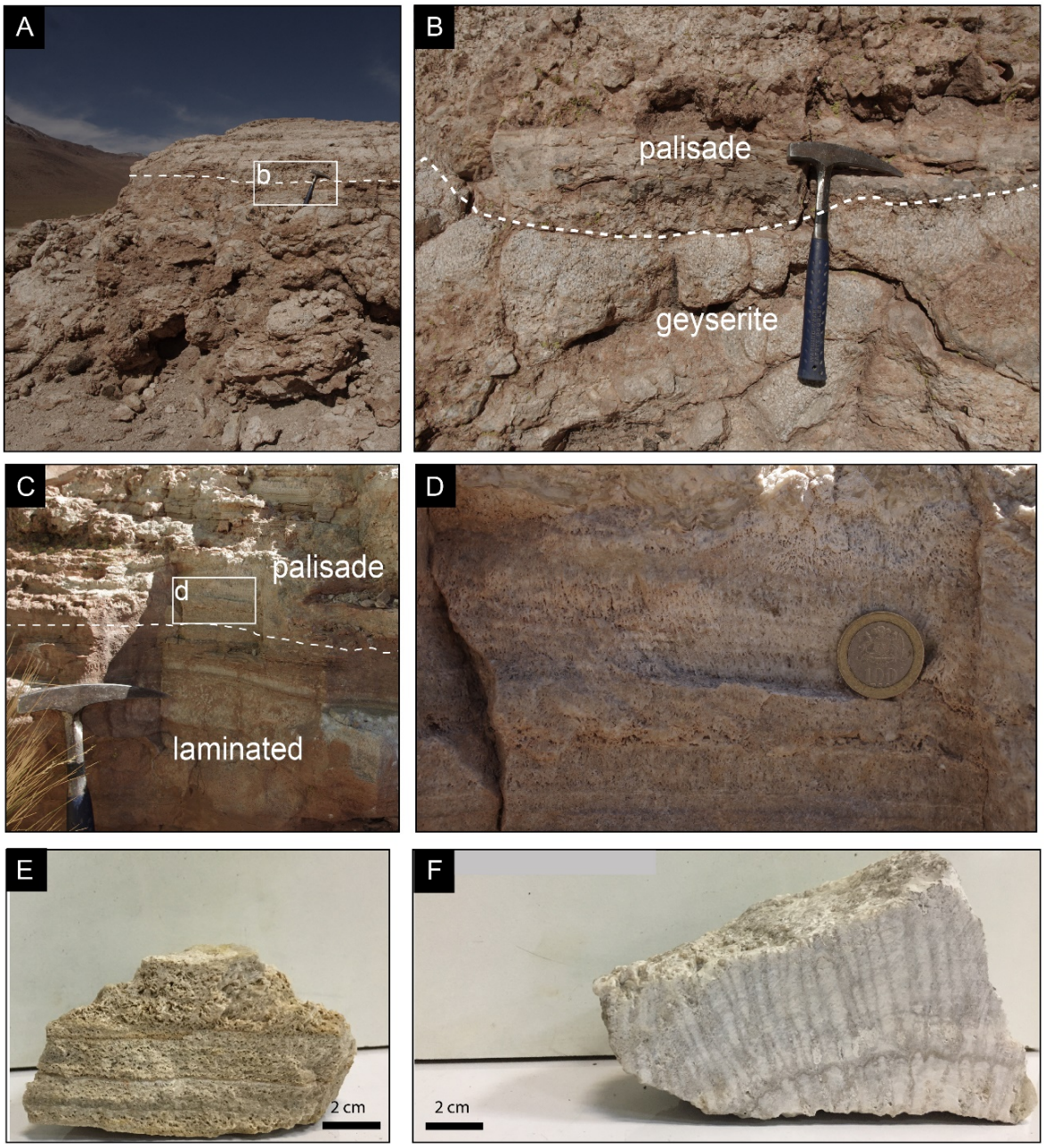

Figure DR2. A and B. Photomicrograph of bacteria filaments present in sample 404d. B. Photomicrograph of bacteria filaments and elongated pores perpendicular to the layering present in sample 408t. C and D. Secondary electron SEM images of filament molds partially filled with porous silica (C: Sample 429t; D: Sample 408t).

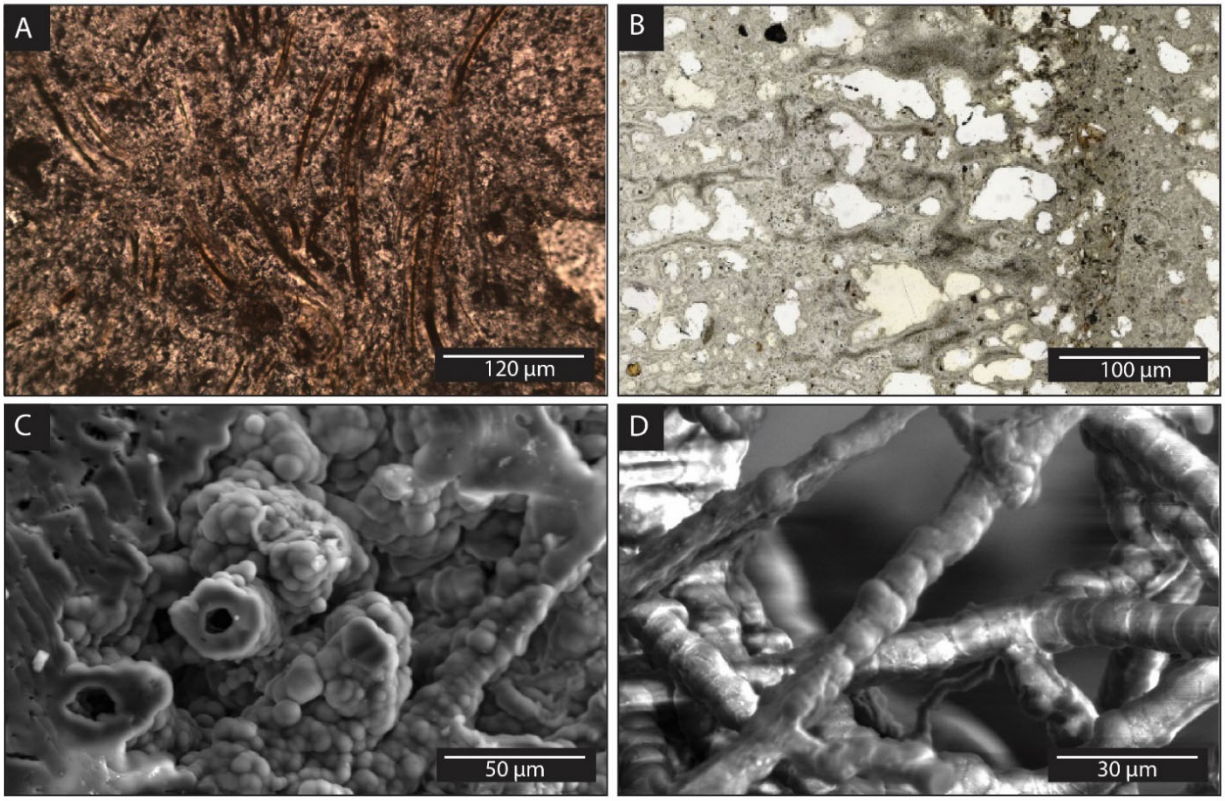

Figure DR3. A and B. Photomicrograph of plant fragments present in sample 429t. C and D. Secondary electron SEM images of plant fragments in sample 404c.

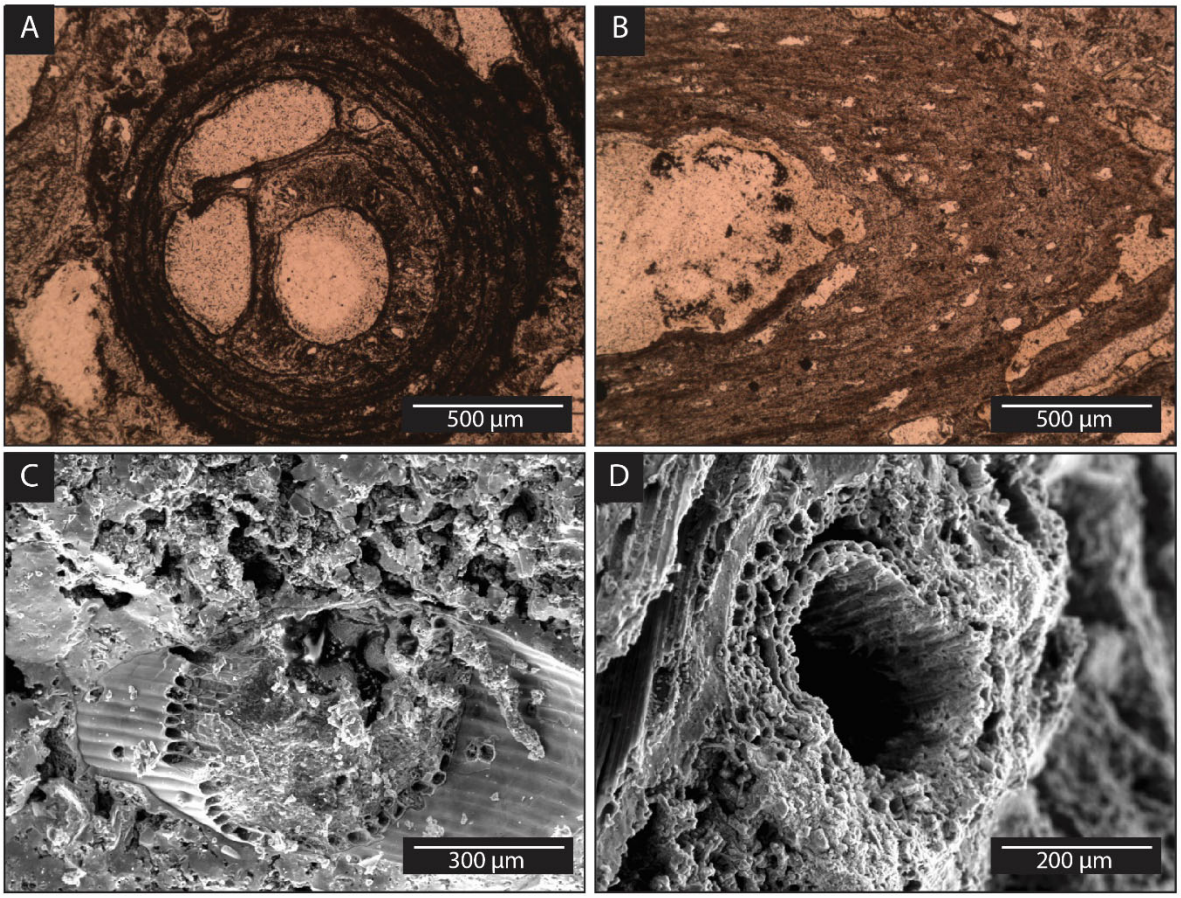

Figure DR4. XRD spectra of selected sinter samples. A. 404 B. 408 C. 429 D. 502. Samples 404a,b,c,d 408b,t, 429b,t and 502b and m correspond to Opal-A. The broadband is centered at 22.22Θ, with FWHM values between 6.9°2Θ and 9.3°2Θ. Samples 404e,f, and 502b correspond to Opal-A/-CT, and FWHM values vary between 5.7 and 6.1°2Θ. Main accessory minerals phases are labeled and correspond to plagioclase (Plg), halite (Hl), detrital quartz (Qz), tridymite (Trd) and cristobalite (Ctb).

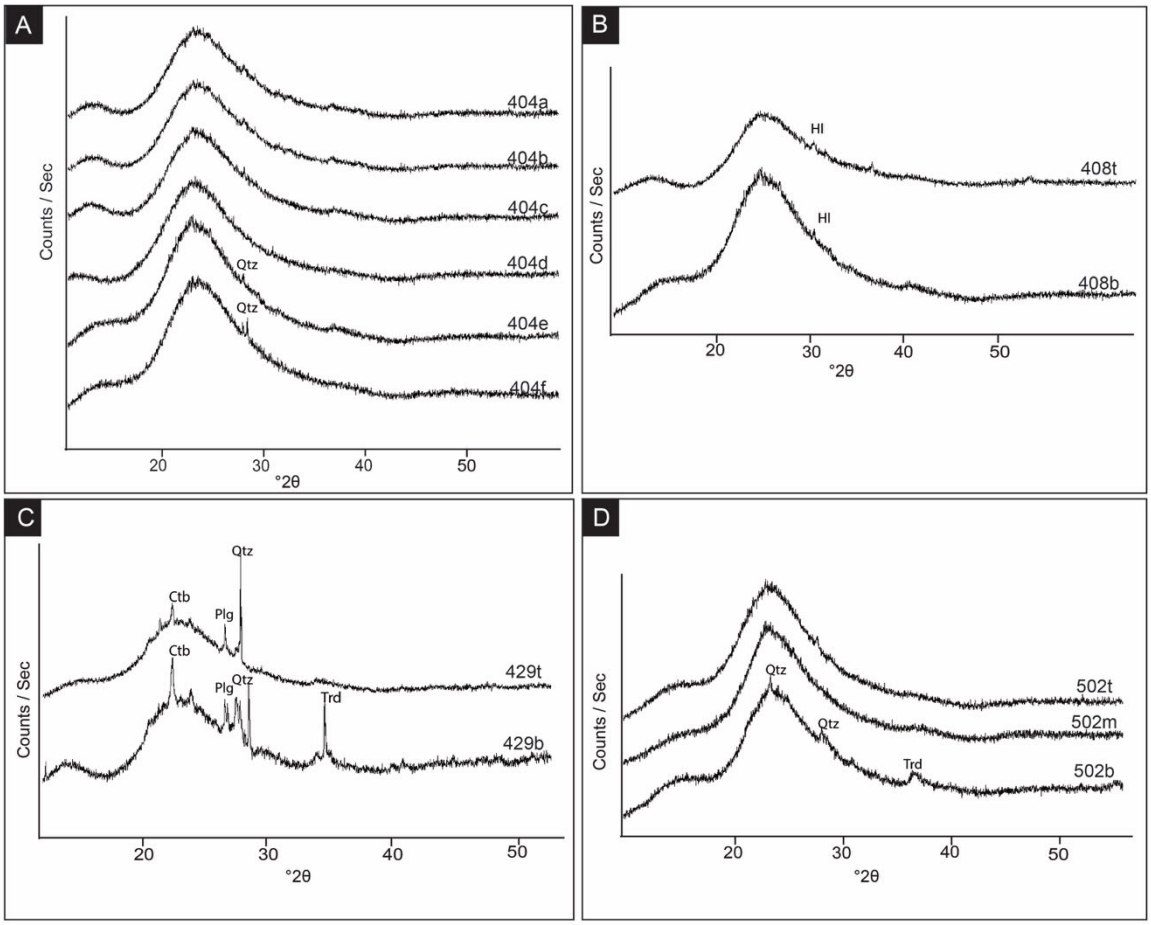

Figure DR5. Paleosinter mounds sampled in this study. Stratigraphic profiles detail sample names and textures. h.a.s.b.: height above section base. A.404 B.408 (modified from Munoz-Saez et al., 2016) C.429 D.502. Stars represent sampling sites for dated sinter.

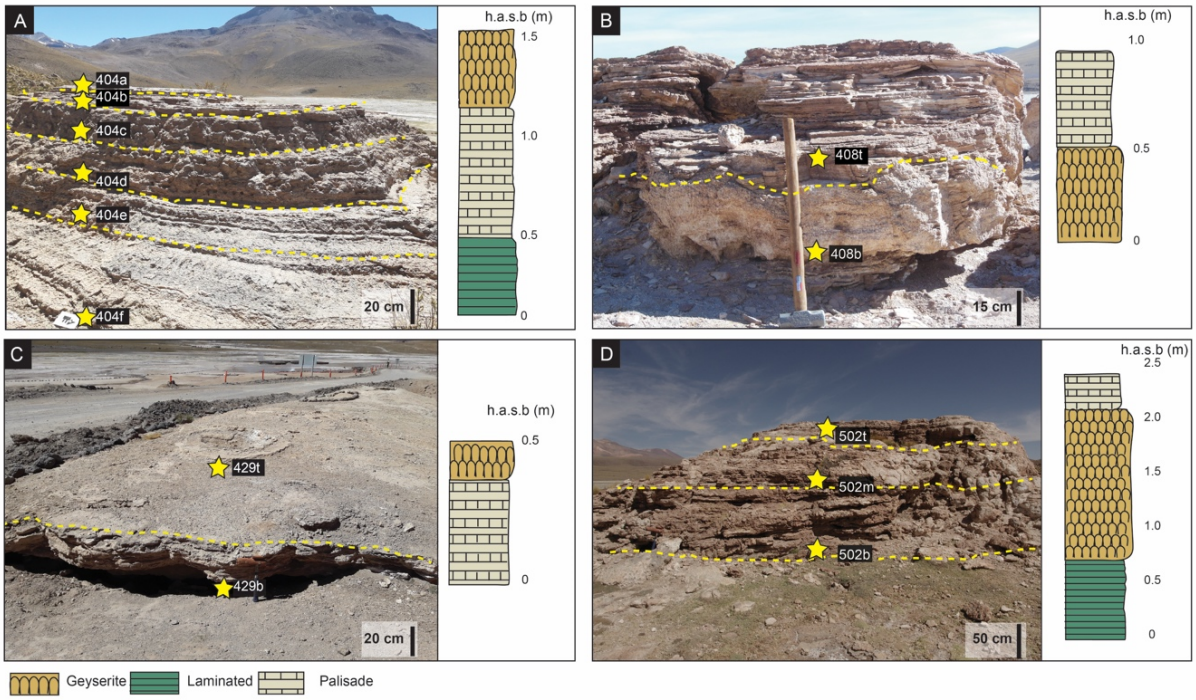

Figure DR6. *In situ* silica precipitation experiments. A, B and C correspond to geyser 411. B is a thermal image of A, obtained with FLIR camera. C is an increased magnification image of the red rectangle in A, showing the set-up of the experiment with sandpaper bands on November 2017. See lens cap for scale (55mm diameter). D, E, and F correspond to geyser 412. E is a thermal image of D, obtained with FLIR camera. F is a close up of the rectangle in D, showing the outflow zone where sandpapers were placed. See coin for scale.

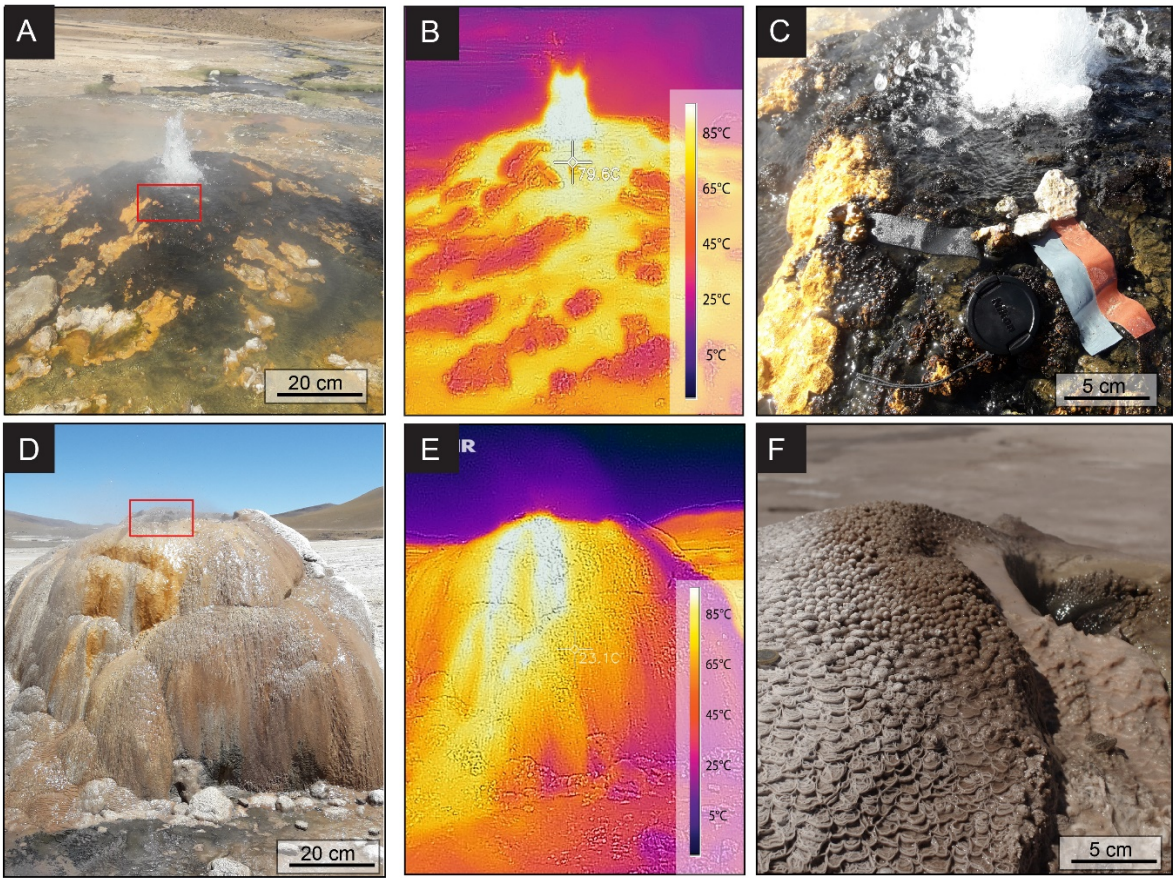

Figure DR7.A. Local weather data of the El Tatio Hydrothermal Field from Jan 26 to April 27, 2018, collected at 2-hour intervals. Top: wind speed vs. air temperature. Bottom: the same wind speed vs. air relative humidity. B. Local weather data of the El Tatio Hydrothermal Field from Jan 26 to 27, 2018 at 10-minute intervals. Top: wind speed vs. air temperature. Bottom: the same wind speed vs. air relative humidity. Respective sunrise and sunset times were indicated by the dash lines and night times were shaded in gray.

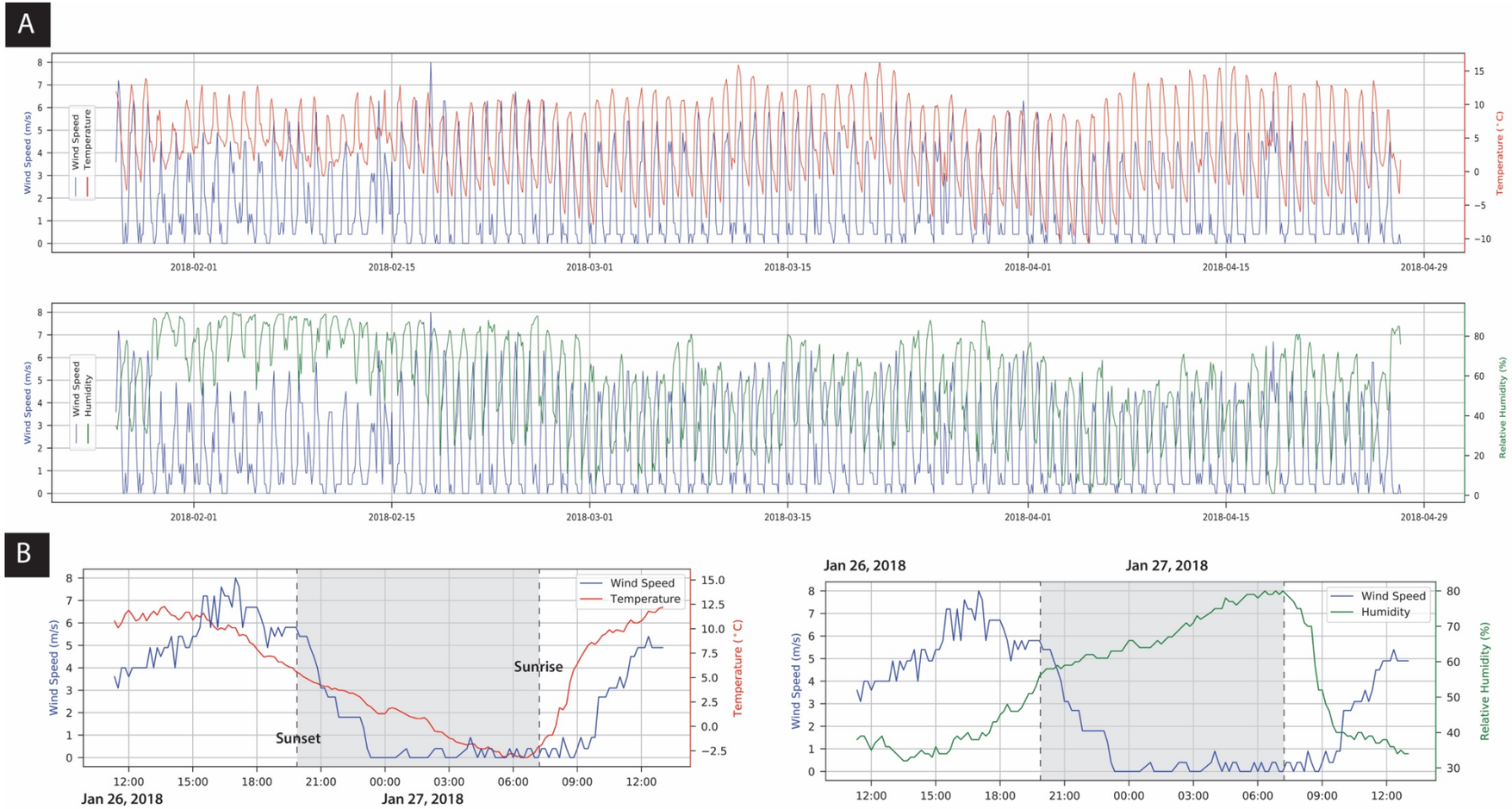
A
Wind Speed (m/s)
Temperature (°C)
Wind Speed
Temperature
2018-02-01
2018-02-15
2018-03-01
2018-03-15
2018-04-01
2018-04-15
2018-04-29
Relative Humidity (%)
Humidity
B
Wind Speed
Temperature
Sunset
Sunrise
Jan 26, 2018
Jan 27, 2018
Humidity

TABLE DR1. RADIOCARBON AGES

Sample code	Lab code	Fraction modern	±	$\delta^{13}C$ (‰)	±	^{14}C age yr BP	±	cal age * cal yr BP		Median probability
404a	198595	0.482	0.0012	-24.03	0.1	5860	25	6527	6696	6626
404b	198596	0.454	0.0040	N.D.[#]	N.D.[#]	6330	80	6999	7340	7207
404c	198594	0.358	0.0062	N.D.[#]	N.D.[#]	8230	140	8718	9480	9147
404d	198611	0.344	0.0020	N.D.[#]	N.D.[#]	8550	50	9437	9548	9506
404e	198613	0.312	0.0010	N.D.[#]	N.D.[#]	9340	30	10375	10588	10501
404e[†]	198593	0.304	0.0014	-25.12	0.1	9565	40	10666	10892	10856
404f	198612	0.259	0.0009	N.D.[#]	N.D.[#]	10840	30	12683	12744	12711
502t	198602	0.971	0.0037	N.D.[#]	N.D.[#]	230	35	139	230	197
502m	198601	0.806	0.0014	-20.42	0.1	1730	15	1540	1613	1585
502m[†]	198618	0.799	0.0014	N.D.[#]	N.D.[#]	1805	15	1611	1673	1648
502b	198600	0.758	0.0014	-20.51	0.1	2220	15	2221	2307	2241
408t	198614	0.933	0.0018	-25.02	0.1	555	20	511	548	531
408b	191794	0.407	0.0022	N.D.[#]	N.D.[#]	7220	45	7930	8065	7993
429t	198617	0.721	0.0014	-22.41	0.1	2625	20	2700	2764	2737
429b	191803	0.629	0.0052	-21.07	0.1	3720	70	3832	4236	4015

*Using the SHCal13 dataset (Hogg et al., 2013). Calibrated ages are presented as mean ages with 2 sigma (95%) confidence limits

[†]Duplicate

[#]N.D= not determined

TABLE DR2. PRECIPITATION RATES BASED ON RADIOCARBON DATA

Lab code	Sample	Texture	Bottom	Top	Thickness (m)	^{14}C age	±	ΔT (yrs)	Area (m^2)	Volume (m^3)	Density (kg/m^3)[§]	Mass (kg)	kg/m^2	Precipitation rate kg/yr per m^2	mm/yr
198600	502b (bottom)	laminated	0	0.7	0.7	2220	15	490	56	39.2	1800	70560	1260	**2.57**	**1.42**
198601	502m	geyserite	0.7	1.9	1.2	1730	15	1500	52	67.2	1800	120960	2160	**1.44**	**0.8**
198618	502m[†]					1805	15				1800				
198602	502t (top)	palisade	1.9	2.4	0.5	230	35		50	28	1800	50400	900		
				Height	2.4										
198612	404f (bottom)	laminated	0	0.7	0.7	10840	30	1275	46	32.2	1800	57960	1260	**0.988**	**0.549**
198613	404e	laminated	0.7	0.9	0.2	9340	30	1015	44	8.8	1800	15840	360	**0.355**	**0.197**
198593	404e[†]					9565	40				1800				
198611	404d	palisade	0.9	1	0.1	8550	50	320	43	4.4	1800	7920	180	**0.563**	**0.313**
198594	404c	palisade	1	1.2	0.2	8230	140	1900	42	8.8	1800	15840	360	**0.189**	**0.105**
198596	404b	palisade	1.2	1.3	0.1	6330	80	470	41	4.4	1800	7920	180	**0.383**	**0.213**
198595	404a (top)	geyserite	1.3	1.5	0.2	5860	25	5860		8.8	1800	15840	360		**0.034**
				Height	1.5										
191803	429b (bottom)	palisade	0	0.3	0.3	3720	70	1095	22	6.6	1800	11880	540	**0.49**	**0.274**
198617	429t (top)	geyserite	0.3	0.5	0.2	2625	20			4.4	1800	7920	360		
				Height	0.5										
191794	408b (bottom)	geyserite	0	0.5	0.5	7220	45	6665	51	25.5	1800	45900	900	**0.14**	**0.075**
198614	408t (top)	palisade	0.5	0.5	0.8	555	20			40.8	1800	73440	1440		
				Height	0.8										

[†] duplicate
[§] (Herdianita et al., 2000)

TABLE DR3. PRECIPITATION RATES BASED ON *IN SITU* EXPERIMENTS

Sample	Longitude	Latitude	Original weight (g)	Total weight (g)	Area (m^2)	Weight (g)/6 months	Weight (g)/1 year	Weight (kg)/ 1 year	kg/yr per m^2
412 a	68°0′32′′W	22°19′41′′ S	0,9381	2,5913	0,0025	1,6532	3,3064	0,0033064	1,32256
412 b	68°0′32′′W	22°19′41′′ S	1,2	4,3729	0,0025	3,1729	6,3458	0,0063458	2,53832
412 c	68°0′32′′W	22°19′41′′ S	1,37	2,4232	0,0025	1,0532	2,1064	0,0021064	0,84256
411 a	68°2′46′′W	22°20′30′′ S	0,9381	4,0892	0,0025	3,1511	6,3022	0,0063022	2,52088
411 b	68°2′46′′W	22°20′30′′ S	1,2	4,8501	0,0025	3,6501	7,3002	0,0073002	2,92008
411 c	68°2′46′′W	22°20′30′′ S	1,37	2,6972	0,0025	1,3272	2,6544	0,0026544	1,06176

TABLE DR4. SILICA SATURATION

Site	SiO_2 (ppm)	T (°C)	log k*	k	SiO_2 sat. ratio
411	283	78.8	-2.32	0.0047	0.99
412	113	75.3	-2.34	0.0045	0.42

*log(K)=-8.476 - 485.24 ·T-1 - 2.268·10-6 ·T2 +3.068 · log(T)

SUPPLEMENTARY TEXT

Radiocarbon ages

Thirteen sinter samples were cut, cleaned, and grinded. The fine-grained samples were later treated with 1 N HCl for 24 h and rinsed with ultrapure water. Then, all samples were digested in 48% HF. The remaining carbonaceous (non-soluble) material was rinsed with ultrapure water and centrifuged. The supernatant was discarded and the carbonaceous precipitate was rinsed with ultrapure water several times. The samples were analyzed for ^{14}C at the UC Irvine Keck-CCAMS facility. The age is reported as before present (BP), where present is AD 1950 (Stuiver and Polach, 1977). Calibrated ages obtained on CALIB (http://calib.qub.ac.uk) using the SHCal13 dataset (Hogg et al., 2013) are also reported. Calibrated ages are presented as mean ages with a 2σ confidence level. All results were corrected for isotopic fractionation using $\delta^{13}C$ values measured with the AMS spectrometer, but these may differ from the isotope ratios of the original material due to fractionation during AMS sample preparation and/or the measurement itself, and are not reported. However, seven samples had a sufficient quantity of carbon collected from the combustion to prepare a separate aliquot of CO_2 for $\delta^{13}C$ analysis, by stable isotope ratio mass spectrometer (IRMS). $\delta^{13}C$ values for those samples were measured to a precision of <0.1‰ relative to PDB, using a Thermo Finnigan Delta Plus IRMS with Gas Bench input at UC Irvine (Table DR1).

X-ray diffraction

Powder X-ray diffraction (XRD) was used to identify silica phases and accessory minerals according to established protocols (Herdianita et al., 2000; Lynne et al., 2007). The analyses were carried out using a Siemens Diffractometer model D-5000 at the Physics Department of the Universidad de Chile. The untreated powder samples (<200 mm) were scanned at a rate of

0.6°2/min, with a step size of 0.01°, from 0 to 40°2, and operating conditions of 40 kV and 30 mA. Accessory minerals were identified using the XPowder12 software. In all diffractograms, the value of the Full Width at Half Maximum (FWHM) was measured by fitting the curve and baseline manually (Lynne et al., 2007). The FWHM is the main parameter used to determine the degree of structural disorder in different non- crystalline silica (Smith, 1998; Lynne et al., 2007).

Samples consist mainly of opal-A, in agreement with previous studies (Fernandez-Turiel et al., 2005; Garcia-Valles et al., 2008; Nicolau et al, 2014). Opal-A/-CT was recognized in samples 404 e and f, and 502b. FWHM values range from 6.9°2Θ to 9.3°2Θ (Fig. DR4), in agreement with Garcia-Valles (2008) (5.7 and 10.6 Δ°2θ), independent of fabric type, being similar among all samples. Higher values have been reported by Nicolau et al. (2014), reaching 12°2Θ, placing El Tatio as the sinter with the highest structural disorder. This particular feature has been attributed to cation incorporation into the silica structure and/or the occurrence of micro- to nano-scale accessory minerals, related to high evaporation conditions (Nicolau et al., 2014; Sanchez-Yañez et al., 2017). In general, values of FWHM decrease with increasing sample age in geyser mounds reaching a difference of 2°2Θ between the bottom and the top, varying from opal-A to opal A-CT. However, these changes cannot be extrapolated to other mounds. For instance, the youngest sample does not present the wider FWHM (Fig. DR4). Our results show that opal-A may persist over time, until 8 ka BP. Certainly, the FWHM changes observed in mounds 404 and 502 in the present study are consistent with the pattern of behavior found by Herdianita et al. (2000), Smith et al., (2003) and Lynne et al., (2007), who reported an overall decrease in FWHM with time. However, its maturation varies from deposit to deposit, probably resulting from different discharge conditions, and therefore, variability in the dissolution-reprecipitation processes. Overall, these sinters are still mineralogically immature.

In situ experiment

The experiments consisted in placing three 25 cm^2 sandpaper sheets that represent a natural rough surface near-vent areas of each site (Fig. 2C). The experiments were performed from November 2017 to April 2018. The mineralized sandpaper sheets were collected and placed into sterilized plastic tubes, and then dried at room temperature. The sheet/silica samples were weighted, and the amount of precipitated silica was determined by subtracting the sandpaper sheet weight from the dried sheet/silica sample. The water temperature at site 411 and 412 were 78.8 °C and 75.3 °C, respectively (Fig. 2D; Fig. DR6). At each site, the thermal water was filtered using a 0.45 µm millipore membrane and then collected in 125 ml bottles. Water samples were analyzed for dissolved silica, using inductively coupled plasma optical emission spectrometry (ICP-OES). The concentration of dissolved SiO_2 at sites 411 and 412 was 283 mg/L and 113 mg/L, respectively.

The significantly higher precipitation rates reported at Wairakei (maximum of 350 kg/yr/m^2; Mountain et al., 2003) and Reykjanes (maximum of 304 kg/yr/ m^2; Tobler et al., 2008) were obtained from wastewater drains at geothermal power plants and hence, do not represent natural discharges. Also, *in situ* studies undertaken at the Map of Australia Pool, at Orakei Korako, Taupo Volcanic Zone, display high precipitation rates (Lynne et al., 2019). In this study, samples were taken from discharge channels covered by a plastic pipe, aiming at comparing the precipitation rate on glass slides with mass flow of geothermal fluids. At Yellowstone National Park, USA some studies focussed on calcite precipitation and the formation of travertine (Blank et al., 2002; Spear et al., 2005; Kandianis et al., 2008 and references therein), and did not present sinter growth rates studies. At Dagunguo hot spring, in China, Peng and Jones (2012) documented opal-A accumulated at rates of 0.5 to 0.75 mm/month in an artificial hot pool and higher values in PVC pipes. We did not include these data in our study because they do not represent natural discharges. In addition, tephrochronological ages were obtained at Geysir, Iceland, intercalated with silica, but no precise silica sinter precipitation rates could be obtained to compare with our data (Jones et al., 2007).

Scanning Electron Microscopy

In order to obtain morphological and textural data, sinter samples were examined using a FEI Quanta 250 Scanning Electron Microscope (SEM) at the Universidad de Chile. The SEM is equipped with secondary electron (SE), energy-dispersive X-ray spectrometry (EDS), backscattered electron (BSE) and cathodoluminescence (CL) detectors. The analyses were performed using a spot size of 1 to 3 m, an accelerating voltage of 5 to 20 keV, a beam intensity of 80 mA, and a working distance of 10 mm.

Aerial Drone Imaging

The aerial images were acquired using DJI Mavic Pro drone with the on-board camera at 12MP resolution. Images were recorded from a height between 20 and 33 meters with sufficient overlaps (>85%). This ensures that every point on the surface was captured more than 5 times (downstream software image processing then chooses the sharpest pixels out of these overlapping images to generate a combined final 2D or 3D map). The images were stitched together using the commercially available Pix4D Mapping Software to combine all images into a map with a resolution better than 1.0 cm/pixel.

Meteorological Data

Meteorological data including temperature, wind speed and relative humidity were collected with a weather station (Vantage Vue, Davis Instruments Co., Hayward, California, USA) that was installed on site near the entrance (22°21'3.38"S, 68° 0'54.21"W), which is about 1 km away from the main hydrothermal field. Short-term meteorological data were collected for one full day from Jan 26 to 27, 2018 at 10-minute intervals and long-term data were collected continuously from Jan 27, 2018, until April 27, 2018, at 2-hour intervals. Local sunrise and sunset times were retrieved from < https://www.timeanddate.com/sun/> on Jan 21, 2019.

The 10-minute interval meteorological data from Jan 26 to 27, 2018 (Fig. DR7A) revealed that local air temperature rises immediately following sunrise to between 10 to 13 °C at noon. This maximum day temperature is near-constant all year round (Fernandez-Turiel et al., 2005). Wind speed shows a consistent ~2 hours lag after the air temperature increase, indicating that wind generation is likely linked to solar heating which warmed the air in the first place. Relative humidity of the air decreased rapidly following sunrise, coinciding in time with the local wind generation, indicating that the local humid air (which accumulated over the night while wind speed is low) is quickly displaced by dry, regional air through wind action. Wind speed reaches to a maximum between 2-6 pm, while the air temperature is high and humidity is low, suggesting that all three factors combine to produce the maximum effect of the evaporation of the hydrothermal fluid as well as the depositing solid sinter material. Long-term meteorological data (Fig. DR7B) further confirms this daily trend, showing that sinter deposition across the El Tatio region likely experiences the same fashion of evaporative drying on a daily basis driven by regional atmospheric processes.

References

Blank, C.E., Cady, S.L., Pace, N.R., 2002, Microbial composition of near-boiling silica- depositing thermal springs throughout Yellowstone National Park: Appl. Environ. Microbiol. 68, 5123–5135

Fernandez-Turiel, J.L., Garcia-Valles, M., Gimeno-Torrente, D., Saavedra-Alonso, J., Martinez-Manent, S., 2005, The hot spring and geyser sinters of el Tatio, northern Chile: Sediment. Geol., v. 180, p. 125–147.

Garcia-Valles, M., Fernandez-Turiel, J.L., Gimeno-Torrente, D., Saavedra-Alonso, J., Martinez-Manet, S., 2008, Mineralogical characterization of silica sinters from the el Tatio geothermal field, Chile: Am. Mineralogist, v. 93, p. 1373–1383.

Herdianita, N.R., Browne, P.R.L., Rodgers, K.A., and Campbell, K.A., 2000, Mineralogical and textural changes accompanying ageing of silica sinter: Mineralium Deposita, v. 35, p. 48–62.

Hogg, A., Hua, Q., Blackwell, P.G., Niu, M., Buck, C.E., Guilderson, T.P., Heaton, T.J., Palmer, J.G., Reimer, P.J., Reimer, R.W., Turney, C.S.M., Zimmerman, S.R.H., 2013, SHCal13 Southern Hemisphere calibration, 0–50,000 years cal BP: Radiocarbon, v. 55, p. 1889–1903.

Jones, B., Renaut, R.W., Torfason, H., Bernhart Owen, R., 2007, The geological history of Geysir, Iceland: a tephrochronological approach to the dating of sinter: Journal of the Geological Society, London, v. 164, p. 1241–1252.

Kandianis, M.T., Fouke, B.W., Johnson, W., Veysey II, J., Inskeep, W.P., 2008, Microbial biomass: a catalyst for CaCO3 precipitation in advection-dominated transport regimes: GSA Bull., v. 120, p. 442–450.

Lynne, B.Y., Campbell, K.A., James, B., Browne, P.R.L., Moore, J.N., 2007, Tracking crystallinity in siliceous hot-spring deposits: American Journal of Science, v. 307, p. 612–641.

Lynne, B. Y., Boudreau, A., Smith, I. J., Smith G. J., 2019, Silica accumulation rates for siliceous sinter at Orakei Korako geothermal field, Taupo Volcanic Zone, New Zealand: Geothermics, v. 78, p. 50-61.

Mountain, B.W., Benning, L.G., Boerema, J.A., 2003, Experimental studies on New Zealand hot spring sinters: rates of growth and textural development: Can. J. Earth Sci. v. 40, p. 1643–1699.

Munoz-Saez, C., Saltiel, S., Manga, M., Nguyen, C., Gonnermann, H., 2016, Physical and hydraulic properties of modern sinter deposits: El Tatio, Atacama: Journal of Volcanology and Geothermal Research, v. 325, p. 156-168.

Nicolau, C., Reich, M., Lynne, B., 2014, Physico-chemical and environmental controls on siliceous sinter formation at the high-altitude El Tatio geothermal field, Chile: Journal of Volcanology and Geothermal Resources, v. 282, p. 60–76.

Peng, X., Jones, B., 2012, Rapid precipitation of silica (opal-A) disguises evidence of biogenicity in high-temperature geothermal deposits: case study from Dagunguo hot spring. China: Sedimentary Geology, v. 257, p. 45–62.

Sanchez-Yañez, C., Reich, M., Leisen, M., Morata, D., Barra, F., 2017, Geochemistry of metals and metalloids in siliceous sinter deposits: Implications for elemental partitioning into silica phases: Applied Geochemistry, v. 80, p. 112-123.

Smith, D.K., 1998, Opal, cristobalite, and tridymite: noncrystallinity versus crystallinity, nomenclature of the silica minerals and bibliography: Powder Diffraction, v. 13, p. 2–19.

Smith, B.Y., Turner, S.J., Rodgers, K.A., 2003, Opal-A and associated microbes from Wairakei, New Zealand: the first 300 days: Mineral. Mag. v. 67, p. 563–579.

Spear, J.W., Walker, J.J., McCollom, T.M., Pace, N.R., 2005. Hydrogen and bioenergetics in the Yellowstone geothermal ecosystem: Proc. Natl. Acad. Sci. U. S. A. v. 102, p. 2555–2560.

Stuiver, M., Polach, H.A., 1977, Discussion: reporting of 14C data: Radiocarbon, v. 19, p. 355–363.

Tobler, D.J., Stefansson, A., Benning, L.G., 2008, In situ grown silica sinters in Icelandic geothermal areas: Geobiology, v. 6, p. 481–502.